PAPER

Check for updates

Supramolecular engineering of cathode materials for aqueous zinc-ion hybrid supercapacitors: novel thiophene-bridged donor–acceptor sp^2 carbon-linked polymers†

Haijun Peng,[a] Verónica Montes-García, [ID] [a] Jésus Raya,[b] Hanlin Wang,[a] Haipeng Guo,[a] Fanny Richard,[a] Paolo Samorì [ID] *[a] and Artur Ciesielski [ID] *[a]

Rechargeable aqueous zinc-ion hybrid supercapacitors (Zn-HSCs) are promising candidates as large-scale energy storage devices owing to their high electrochemical performance, safety, long life, and low price. The development of nanostructured electrode materials featuring multiple active sites capable of interacting with Zn ions represents an efficient strategy to boost their electrochemical performance. In this work, we report for the first time the use of donor–acceptor carbon-linked conjugated polymers (DA-CCPs) as cathodes in aqueous Zn-HSCs. We have synthesized two novel DA-CCPs *via* Knoevenagel polymerization between electron-accepting 2,2′,2″-(benzene-1,3,5-triyl)triacetonitrile and electron-donating 2,5-thiophene dicarboxaldehyde or [2,2′-bithiophene]-5,5′-dicarboxaldehyde, yielding DA-CCP-1 and DA-CCP-2, respectively. DA-CCP-2, which possesses an extra-thiophene unit in the backbone, exhibits improved electrochemical characteristics when compared to DA-CCP-1, and performance surpassing those of other reported cathode materials for aqueous Zn^{2+} energy storage systems. DA-CCP-1 and -2 based electrodes exhibited an outstanding energy density of 80.6 and 196.3 W h kg^{-1} respectively, representing the highest value ever reached for conjugated polymers to date. This study not only offers new perspectives for the rational design and precise synthesis of DA-CCPs but it also broadens the choice of cathodes for high-performance aqueous Zn-HSCs.

Introduction

While our society is facing an ever-increasing energy need to power all digital tools that characterize our daily life, the shortage of critical raw materials (CRMs) forces scientists to devise new means for energy generation and storage. In view of the portability of today's electronics, novel, highly efficient and sustainable energy storage systems (ESSs) are highly sought after.[1–3] Since 1991, lithium-ion batteries (LIBs) have attracted enormous research interest due to their high energy density and low self-discharge.[4,5] However, the safety concerns caused by the flammable organic electrolytes and their low power density hamper the application of LIBs in fields where fast and high-power density storage devices are required, such as in automobiles.[6,7] Supercapacitors (SCs) represent most promising alternatives to currently market-dominating technologies as

they can drastically reduce or even eliminate the use of CRMs (*e.g.*, Li, Co and natural graphite).[8] SC technology does not require any fire protection as it is not susceptible to thermal runaway during charging/discharging processes that are merely based on electrostatic forces and not on chemical reactions that involve ion diffusion processes. However, a major drawback of SCs is the low energy density of commercially available SCs (10–12 W h kg^{-1}, 5–8 W h L^{-1}) when compared to LiBs (>100 W h kg^{-1}). Therefore, the performance of active materials incorporated in SCs' electrodes and electrolytes must be further improved in order to increase the energy density of SCs. On the one hand, the use of novel nanostructured electrode materials and their engineering through physical blending or chemical functionalization incorporating numerous redox-active groups can substantially enhance the energy density of SCs, approaching the values of batteries.[9] On the other hand, battery and capacitor-type electrodes can be combined in a single device, known as hybrid supercapacitors (HSCs) in order to gain the merits and to offset the specific problems faced both by batteries and SCs.[10–12] Although Li-ion hybrid SCs have been extensively studied in the past few decades,[13–15] in 2020 Li was identified for the first time as a CRM,[16] sparking the development of new ESSs relying on Na$^+$, K$^+$, Mg$^+$, Al^{3+}, Zn^{2+}, *etc.*[17] The

[a]Université de Strasbourg, CNRS, Institut de Science et d'Ingénierie Supramoléculaires, 8 allée Gaspard Monge, Strasbourg 67000, France. E-mail: samori@unistra.fr; ciesielski@unistra.fr

[b]Université de Strasbourg, CNRS, Membrane Biophysics and NMR, Institute of Chemistry, 1 Rue Blaise Pascal, Strasbourg 67000, France

† Electronic supplementary information (ESI) available. See DOI: https://doi.org/10.1039/d2ta09651j

high theoretical capacity of Zn (820 mA h g^{-1}; 5845A h L^{-1}), its low cost (USD \$2 per kg), and its low redox potential (-0.763 V vs. the standard hydrogen electrode) make the Zn anode an ideal candidate for the next generation of ESSs such as rechargeable aqueous zinc-ion hybrid supercapacitors (Zn-HSCs), exhibiting high energy/power density and long lifespan. Moreover, because of the high abundance of Zn resource (like ZnO and ZnS), Zn-HSCs are considered highly sustainable.[18-26] Among the emerging cathode electrode materials, carbon-linked conjugated polymers (CCPs), a subclass of porous organic polymers, are considered as an appealing option because of their higher theoretical capacity, tunable electrochemically active structure, and the in-plane π-conjugation that can facilitate charge transport.[27] Unlike covalent organic frameworks (COFs), whose growth is governed by thermodynamics and typically yields in high crystallinity of materials yet via time consuming synthetic protocols, CCPs can be easily synthesized under mild conditions and display high physicochemical stability in aqueous solvents due to their polycrystalline nature and the formation of irreversible covalent carbon–carbon double bonds (–CC–).[28,29] In addition, as pseudocapacitive materials, CCPs offer a pathway for achieving both high energy and high power densities.[30] Among different CCP designs, the donor–acceptor one is particularly attractive since it enables the modulation of the CCPs' band gap through the chemical tuning of the redox properties of the donor and acceptor moieties.[31-33] For instance, Zhang et al. reported the synthesis of two conducting redox polymers based on anthraquinone and polycarbazole, respectively, and studied their properties–performance relationship. The carbazole-based donor–acceptor copolymer exhibited a wider energy band gap and as a consequence a wider operating voltage range (up to 2.4 V) and a higher energy density (29.1 W h kg^{-1}) when compared to anthraquinone-based copolymers.[34] Different strategies have been explored to improve the electrochemical performance of conjugated polymers in symmetric SCs such as the use of donor–acceptor–donor (D–A–D) building blocks[32] or the synthesis of p/n-doped conjugated polymers.[34] While in some cases the potential windows were extended above 2 V, the obtained energy values never exceeded 30 W h kg^{-1}. Compared with conjugated polymer frameworks, CCPs display a higher chemical stability and enhanced delocalized electronic structures. Although CCPs have been used in optoelectronic devices with enhanced photostability,[35] for high-efficiency photocatalytic hydrogen evolution,[36] or as photocathodes for water reduction,[37] their application as energy storage materials has been barely explored.[38] Feng et al. reported a novel 2D CCP via the condensation of 1,4-phenylenediacetonitrile with the redoxactive hexaazatrinaphthalene (HATN) derivative.[38] Their effective hybridization with a conductive material, i.e., carbon nanotubes, allowed for their use as cathode materials in lithium-ion batteries (LIBs) and they demonstrated a high capacity of 116 mA h g^{-1}, excellent cycling stability, and rate capability.[38] However, to the best of our knowledge, the use of CCPs as cathode materials in HSCs remains unexplored. The synergistic combination of all the physicochemical properties of CCPs, 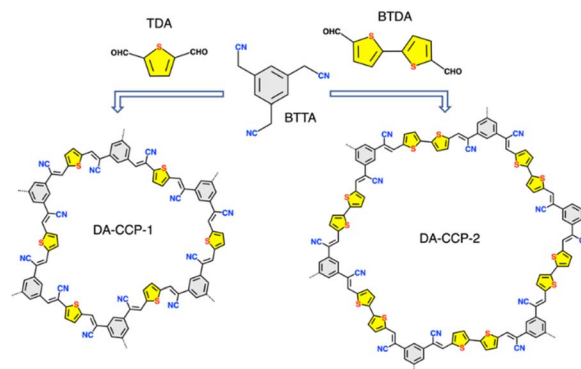together with the hybrid device configuration, will serve as an ultimate strategy for the development of high-energy and high-power HSC devices.[39,40]

Herein, we report the synthesis of two novel thiophene-bridged donor–acceptor CCPs via Knoevenagel polymerization between an electron-accepting building block 2,2′,2″-(benzene-1,3,5-triyl)triacetonitrile (BTAN) and an electron-donating linker 2,5- thiophene dicarboxaldehyde (TDA) and [2,2′-bithiophene]-5,5′-dicarboxaldehyde (BTDA), yielding DA-CCP-1 and DA-CCP-2, respectively. An aqueous Zn-HSC was assembled, in which DA-CCP-1 or DA-CCP-2 and Zn foil were used as the cathode and anode, respectively, while an aqueous solution containing zinc trifluoromethanesulfonate (Zn(CF$_3$SO$_3$)$_2$) served as the electrolyte. The DA-CCP-1 and -2 based Zn-HSCs displayed a high specific capacity of 103.4 and 251.7 mA h g^{-1}, respectively, at a current density of 0.1 A g^{-1}, being according to our knowledge higher than that of other reported COFs and porous carbon-based electrode materials. Remarkably, the DA-CCP-1 and -2 based electrodes exhibited an outstanding maximum energy density of 196.3 and 80.6 W h kg^{-1}, the highest reported energy density value to date for conjugated polymers. Moreover, we revealed for the first time a pseudocapacitive energy storage mechanism through ex situ XPS and FTIR analysis, where the thiophene-S units in DA-CCPs were identified as the electrochemically active sites in the Zn-HSCs.

Results and discussion

The synthetic path employed for the synthesis of DA-CCP-1 and DA-CCP-2 is portrayed in Scheme 1. A Knoevenagel condensation between a C3-symmetry electron-accepting unit, 1,2,2′,2′-(benzene-1,3,5-triyl) triacetonitrile (BTTA), and a linear electron-donating unit, 2,5-thiophene dicarboxaldehyde (TDA) or [2,2′-bithiophene]-5,5′-dicarboxaldehyde (BTDA), was performed through a solvothermal reaction in a closed micro-reaction vessel (see the ESI† for details).

The solid-state nuclear magnetic resonance (NMR) analysis of CCPs is typically performed on the basis of classical ^{13}C cross-polarization magic angle spinning (CP-MAS) experiments.[41-43] However, in solid-state ^{13}C resonances are rather broad and can easily overlap, for instance quaternary (C$_q$) and CH chemical

Scheme 1 Synthesis of DA-CCP-1 and -2 by Knoevenagel polymerization between BTTA and TDA or BTDA.

This journal is © The Royal Society of Chemistry 2023

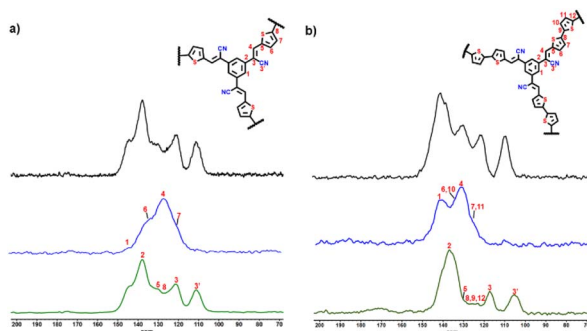J. Mater. Chem. A, 2023, **11**, 2718–2725 | **2719**

Fig. 1 ^{13}C solid-state NMR series of (a) DA-CCP-1 and (b) DA-CCP-2. Bottom (green): edited CP/MAS (only C_q and CH_3 detected); middle (blue) short contact time (45μs) CP/MAS (selects CH and CH_2); top (black): long time (4 ms) regular CP/MAS spectrum (all carbons there).

shifts are located in the same small crowded zone (*ca.* 110 to 150 ppm), making the signals' assignment process burdensome. Therefore, advanced ^{13}C CP-MAS NMR experiments can be performed including ^{13}C spectral edition,[44] enabling more precise assignments by matching the expected chemical shifts to the expected moieties. In the recorded ^{13}C CP-MAS NMR spectra of DA-CCP-1 and -2 (Fig. 1), the chemical shift at ~110 ppm has been assigned to the carbon atoms in cyano groups (–CN),[45] and the chemical shifts at ~119 and ~137 ppm confirm the formation of cyanovinylene [–CHC(CN)–] bridges.[46,47] Furthermore, Fourier transform infrared (FT-IR) spectroscopy (Fig. S4†) revealed the presence of –CN groups in both DA-CCP-1 and -2, which are shifted from ~2250 cm^{-1} (–CH_2CN of BTTA) to ~2197 cm^{-1} [–CHC(CN)– of CCPs]. Moreover, the peak at 1554 cm^{-1} present in both CCPs can be attributed to the vibrations of the olefin-linked CC bond and provides proof for successful Knoevenagel polymerization.[37,48]

The crystallinity of DA-CCP-1 and -2 has been assessed by powder X-ray diffraction (PXRD) measurements (Fig. 2a). Unlike the highly crystalline BTTA, TDA, and BTDA monomers with numerous diffraction peaks, only a broad band at $2\theta = 25°$ has

Fig. 2 (a) XRD spectra of DA-CCP-1 and -2 and their monomers. (b) Optical image of the synthesized DA-CCP-1 and -2. (c) UV/vis absorption spectra of DA-CCP-1 and -2.

been recorded for both DA-CCPs, which is typically attributed to graphitic (002) diffractions, suggesting that DA-CCP-1 and -2 have a layered and polycrystalline nature.[28,47,49]

The optical and electrochemical properties of DA-CCP-1 and -2 have been studied by ultraviolet-visible (UV-vis) spectroscopy and cyclic voltammetry (CV). In contrast to the model compound, which is obtained from the reaction of BTAN with 2-thiophenecarboxaldehyde (Fig. S3†), the mono-thiophene bridged DA-CCP-1 exhibited an absorption band centred at 576 nm, whereas the bithiophene-bridged DA-CCP-2 showed a red-shifted absorption band centred at 632 nm (Fig. 2c), as a result of the more extended conjugation.[45,50] Moreover, Tauc plots (Fig. S5†) are commonly used to calculate the energy bandgap of semiconductors.[51] The measured bandgap (E_g^{opt}) for DA-CCP-1 and -2 amounted to 2.16 and 2.07 eV, respectively. The broader absorption and smaller energy bandgap of DA-CCP-2 were attributed to the greater intramolecular charge transfer from the donor (bithiophene) to the acceptor (BTTA core) moieties.[52] To gain further insight into the frontier energy levels, CV measurements of DA-CCP-1 and -2 were performed (Fig. S6†). The estimated onset reduction and oxidation potentials amounted to ~−0.91 and ~1.2 V, respectively, in reference to the redox potential of ferrocene/ferrocenium (Fig. S7†). The highest occupied molecular orbital (HOMO) and the lowest unoccupied molecular orbital (LUMO) levels of DA-CCP-1 and -2 were extracted (see the ESI† for details) as −5.66/−3.46 eV and −5.50/−3.46 eV, respectively. The HOMO of DA-CCP-1 and -2 was further determined by ultraviolet photoelectron spectroscopy (UPS) as displayed in Fig. S8.† The Fermi level (E_F) according to Einstein's photo-emission law can be determined as follows: $E_F = h\nu - E_{cutoff}$, where the $h\nu$ is the photon energy (21.22 eV here) and the E_{cutoff} represents the secondary electron cut-off edge. E_{cutoff} values are determined to be 3.83 and 4.47 eV and therefore the HOMO values were calculated to be −5.91 and −5.65 eV, respectively, being comparable to the CV calculated results. The resultant band gaps, *i.e.*, 2.20 for DA-CCP-1 and 2.04 eV for DA-CCP-2, provide evidence that both DA-CCPs are semiconductive materials, in full agreement with UV-vis spectroscopy results. The bulk conductivity of DA-CCP-1 and -2 was calculated to be 3.7×10^{-5} and 4.2×10^{-5} S m^{-1}, respectively.

The porosity of DA-CCP-1 and -2 was evaluated by recording N_2 adsorption–desorption isotherms at 77 K (Fig. S9†). The adsorption isotherms of the two polymers exhibited Type-I sorption isotherms, with steep rises appearing at low relative pressure and also Type-IV sorption features with adsorption/desorption hysteresis at higher pressure.[53] The calculated Brunauer–Emmett–Teller (BET) surface area of DA-CCP-1 and -2 amounted to 584 and 674 m^2 g^{-1}, respectively. The pore size distribution analysis results indicated the dominance of micropores in DA-CCP-1 and -2. However, the presence of mesopores was also monitored in DA-CCP-2 (Fig. S10†). The thermogravimetric analysis (TGA) (Fig. S11†) revealed thermal stability for both DA-CCP-1 and -2 at temperature as high as 500 and 400 °C, respectively, which can be attributed to the robustness of the highly cross-linked and rigid polymeric networks. The morphology of DA-CCP-1 and -2 was investigated by scanning electron microscopy (SEM) (Fig. 3 and S12†) and
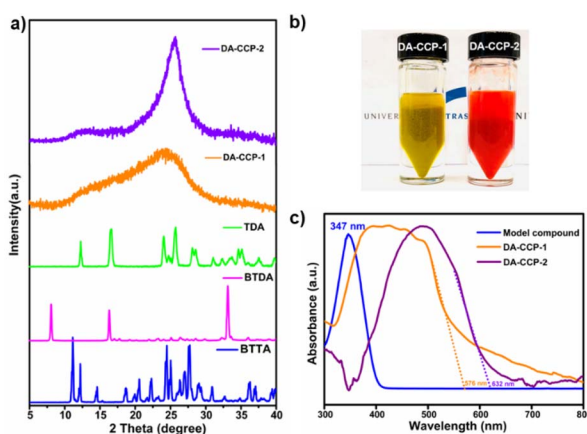
2720 | *J. Mater. Chem. A*, 2023, **11**, 2718–2725

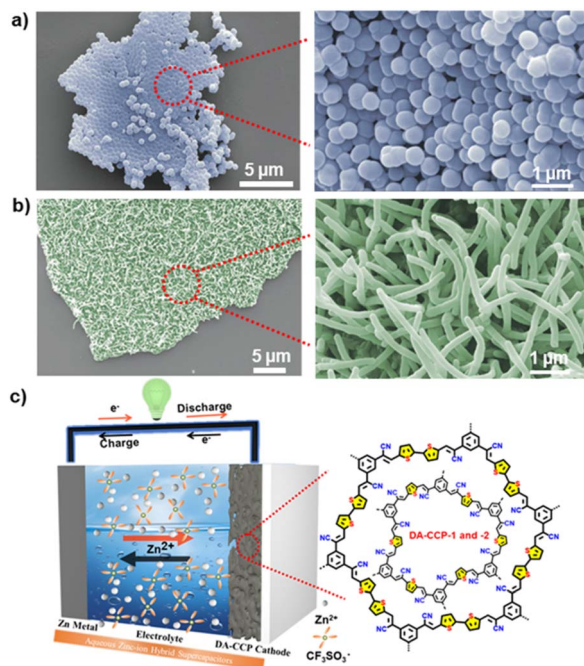This journal is © The Royal Society of Chemistry 2023

Fig. 3 SEM images of (a) DA-CCP-1 and (b) DA-CCP-2. c) Scheme of the CCP//Zn(CF$_3$SO$_3$)$_2$//Zn energy storage system. Herein, DA-CCP-1 or -2 serves as the cathode, Zn foil is used as the anode and 2 M Zn(CF$_3$SO$_3$)$_2$ aqueous solution is employed as the electrolyte.

scanning transmission electron microscopy (STEM) (Fig. S13 and 14†). DA-CCP-1 was composed of spherical nanoparticles with a diameter of ~500 nm (Fig. 3a and S13†), as also confirmed by STEM (Fig. S13†). On the other hand, DA-CCP-2 exhibited micrometer-long fiber-like structures (Fig. 3b), as also visible on the STEM images recorded both in bright and dark fields (Fig. S14†). Interestingly, the subtle difference in the chemical structure, *i.e.*, the presence of one additional thiophene unit in one of the building blocks of DA-CCP-2, resulted in a completely different morphology, demonstrating that the final morphology of CCPs or COFs cannot be predicted *a priori*.

The electrochemical performance of DA-CCP-1 and -2 as cathode electrodes in aqueous Zn-HSCs was then assessed. The Zn^{2+}-ion storage behaviour of the DA-CCP-1 and -2 cathodes was tested by assembling a two-electrode system in Zn-HSC devices by employing a commercial Zn foil anode and 2 M zinc tri-fluoromethanesulfonate (Zn(CF$_3$SO$_3$)$_2$) aqueous electrolyte (Fig. 3c), with detailed experimental conditions provided in the ESI.† Zn(CF$_3$SO$_3$)$_2$ salt in H$_2$O is a common aqueous electrolyte for batteries and SCs.[25] Chen *et al.*[54] revealed that the coulombic efficiency (CE) of zinc batteries when Zn(CF$_3$SO$_3$)$_2$ in aqueous media is used as the electrolyte can gradually reach 100% as a result of the bulky nature of the CF$_3$SO$_3^-$ anions facilitating Zn^{2+} transport and charge transfer. Fig. 4a and d portray the CV profiles of DA-CCP-1 and DA-CCP-2 at a scan rate of 10–1000 mV s^{-1} in the 0 to 1.6 V potential window. The presence of redox peaks for both DA-CCPs at low scan rates denotes the electrode store energy through a faradaic process. A significant increase of the peak current densities with the scan rate suggests good

kinetic characteristics of the Zn^{2+} ion diffusion into the pores of the DA-CCP-1 and DA-CCP-2 electrodes. It is worth mentioned that the anodic and cathodic peaks of DA-CCP-1 shifted to higher and lower potential positions respectively, when increasing the scan rate, which is probably due to an increase in the internal diffusion resistance during the electrochemical reaction.[55] However, the redox peaks of the DA-CCP-2 electrode disappear at higher scan rates than 200 mV s^{-1} because of the insufficient utilization of the active sites available for the migration of electrolyte ions.[56] The kinetics of electrochemical processes occurring at DA-CCP-1 and -2 cathode electrodes were investigated by exploiting the procedure proposed by Wu *et al.*,[57] according to the equation: $I = a\nu^b$, where i represents the current density, ν refers to the scan rate, and a and b are variable parameters. The b-value varies between 0.5 and 1, being closer to 0.5 when the charge storage mechanism is governed by a diffusion-controlled process and closer to 1 when is governed by a capacitive-controlled process. The b-values of DA-CCP-1 and -2 cathodes calculated from the slope of $\log(i) - \log(\nu)$ curves in Fig. S15† amount to 0.67 and 0.69, which indicates that the Zn^{2+} storage mechanism of the DA-CCP-1 and -2 cathodes is dominated by a diffusion contribution with a partial capacitive controlled contribution. This result confirms the coexistence of an electrical double layer (EDL) and battery-type mechanism due to the pseudocapacitive nature provided by the thiophene-type sulphur groups. The adopted potential window for galvanostatic charge–discharge (GCD) measurements was determined by performing CV in different voltage ranges (Fig. S16 and S17†). The DA-CCP-1 and -2 electrodes exhibited quasi rectangular I–V behaviour between 0.2 and 1.6 V with no polarization effects. The GCD profile of DA-CCP-1 and -2 (Fig. 4b and e) in the adopted potential window confirmed that the charge-storage mechanism was not purely faradaic as in typical materials for batteries; the absence of a voltage plateau provided evidence for a hybrid charge-storage behaviour, confirming that both DA-CCP-1 and -2 have to be regarded as pseudocapacitive-type materials. It is noteworthy that several cathode materials have been explored in Zn-HSCs exhibiting hybrid charge-storage properties,[58–61] and the same behaviour was also observed in COF-based Li or Na ion super-capacitors.[62,63] The GCD measurements results in the adopted potential window (0.4–1.6 V) for the DA-CCP-2 (Fig. 4e) cathode displays a significantly higher discharge capacity of 251.7 mA h g^{-1} compared to 103.4 mA h g^{-1} of DA-CCP-1 (Fig. 4b) at a current density of 0.1 A g^{-1}, being superior to most of the reported COF cathodes and inorganic or organic electrode materials (Table S1†). The higher performance of DA-CCP-2 indicates a more efficient utilization of the electrochemically active sites than in DA-CCP-1, which is mainly attributed to the higher surface area and larger pore size of DA-CCP-2 and the synergistic effect of the adjacent pentacyclic thiophene-S units per structural repeating unit. In addition, the capacity of DA-CCP-2 and DA-CCP-1 could remain at 78.5 and 40.2 mA h g^{-1}, respectively, even at a large current density of 5 A g^{-1}. Subsequently, the rate performance of DA-CCP-1 and -2 was analysed at different current densities (Fig. S18 and S19†). A good rate capability was achieved for DA-CCPs where capacity
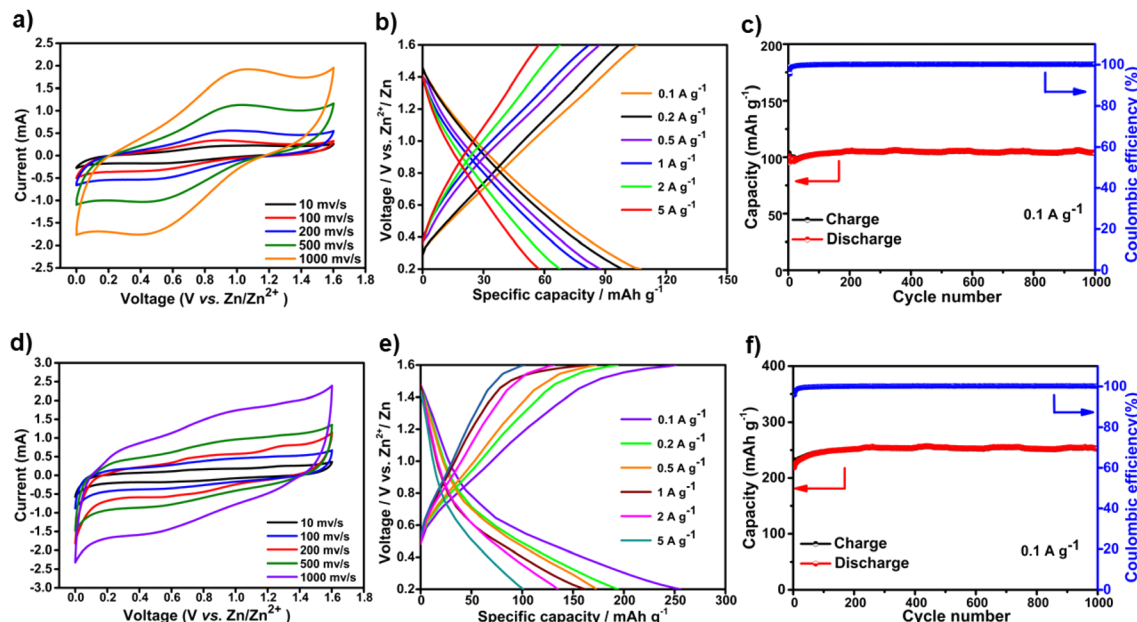
This journal is © The Royal Society of Chemistry 2023

J. Mater. Chem. A, 2023, **11**, 2718–2725 | **2721**

Fig. 4 (a) and (d) Typical CV curves of the DA-CCP-1 and -2 cathodes at different scan rates of 10–1000 mV s^{-1}. (b) and (e) GCD curves of the DA-CCP-1 and -2 cathodes at different current densities. (c) and (f) Cyclability test of DA-CCP-1 and -2 at a current density of 0.1 A g^{-1} for 1000 cycles.

values of 251.7, 193.6, 171.8, 160.7, 131.8, and 101.2 mA h g^{-1} for DA-CCP-2 and 103.4, 97.8, 88.3, 82.2, 70.1, and 57.8 mA h g^{-1} for DA-CCP-1 were obtained at a current density of 0.1, 0.2, 0.5, 1, 2, and 5 A g^{-1}, respectively. Importantly, when the current density decreased to 0.1 A g^{-1}, the specific capacities of 209.2 and 102.8 mA h g^{-1} could be fully recovered, indicating excellent reversibility. Remarkably, the DA-CCP-1 and -2 based electrodes delivered an outstanding maximum energy density of 80.6 and 196.3 W h kg^{-1}, comparable to battery and supercapacitor-level power densities of 8.3 and 20.5 kW kg^{-1}, respectively. These results suggest that the as-prepared DA-CCP-1 and -2 cathode electrodes are ideal candidates for fast energy storage because they exhibited not only rapid kinetics, but also good reversibility of electrochemical reactions. Long charge and discharge tests (Fig. 4c and f) provided evidence for the high cyclability of DA-CCP-1 and -2 electrodes at a high current density of 0.1 A g^{-1}, which can retain 96.2% and 84.5%, respectively, of the initial capacity value after >1000 cycles. Moreover, the coulombic efficiency of the DA-CCP-1 and 2 cells well remained at 99% of its initial value throughout the 1000 charge–discharge cycles. The DA-CCP-1 and -2 based Zn-HSCs exhibited an outstanding electrochemical Zn^{2+} storage performance, including an excellent rate capability, long cycle life, and high energy density and power density. Such unique features resulted from the joint effect of (i) the presence of thiophene units in the frameworks providing rich electrochemically active sites and enabling the optimization of the infiltration of the electrolyte to improve the surface charge storage; (ii) the semiconducting nature of the conjugated skeleton providing charge transfer characteristics and charge/discharge capacities; (iii) the relatively high specific surface area and intrinsic cavity of DA-CCP-1 and -2, combined with

their insoluble nature in aqueous media, offering distinct advantages for fast ion transport through the electroactive materials, as well as overcoming the dissolution issues often encountered in organic batteries and SCs.[64,65]

To further investigate the fast Zn^{2+} electrochemical kinetics of the DA-CCP-1and -2 electrodes, electrochemical impedance spectroscopy (EIS) was carried out. The Nyquist plots (Fig. S20†) displayed the typical shapes of capacitive electrodes, which comprise a semicircle in the high-frequency region revealing the charge-transfer process, and a line in the low-frequency region corresponding to a diffusion process. The diameter of the semicircle in the high-frequency range represents transfer resistance (R_{ct}) (Tables S2 and 3†). DA-CCP-2 exhibited a smaller R_{ct} of about 29 Ω compared with 45 Ω of DA-CCP-1, which suggests a faster electrochemical reaction occurring at the electrode/electrolyte interface of DA-CCP-2. The higher slope in the low-frequency range of DA-CCP-2 also indicated that the DA-CCP-2 electrode exhibits faster ion diffusion.[66]

Energy dispersive X-ray spectroscopy (EDS) analysis was performed to determine the elemental composition of pristine DA-CCP cathodes as well as after 1000 charge/discharge cycles (Fig. S21–S24†). The C, N and S elements were homogeneously distributed on the stainless electrodes, suggesting a uniform spatial distribution of DA-CCPs in the pristine electrodes (Fig. S23†), and the presence of the Zn element after 1000 cycles further proved the Zn^{2+} insertion into the DA-CCP electrodes (Fig. S22 and S24†). Moreover, the SEM images of the DA-CCP-1 and -2 electrodes after 1000 cycles did not show any obvious change in the material's morphology, indicating their high stability during the charge–discharge process (Fig. S25 and S26†).

2722 | *J. Mater. Chem. A*, 2023, **11**, 2718–2725

This journal is © The Royal Society of Chemistry 2023

Ex situ X-ray photoelectron spectroscopy (XPS) analysis was executed to investigate the chemical state of the concerned electrochemically active unit in the pristine, discharged, and charged states of DA-CCP-1 and -2 (Fig. S27–S29†) to provide a deeper understanding of the charge storage mechanism. In pristine compounds, the observed S $2p_{1/2}$ 165.2 eV and S $2p_{3/2}$ 163.9 eV in DA-CCP-1 and S $2p_{1/2}$ 165.5 eV and S $2p_{3/2}$ 164.2 eV in DA-CCP-2 are ascribed to thiophene-type sulphur (thiophene-S).[67,68] In the discharge process (Fig. 5a and b), the Zn^{2+} ions move from the Zn anode to the DA-CCP-1 and -2 based cathodes, and coordinate with thiophene-S by extracting a lone pair of electrons from thiophene-S, forming a Zn-thiophene-S coordination complex. This complex formation resulted in a chemical shift to a higher binding energy of S $2p_{1/2}^*$ 170.8 eV, S $2p_{3/2}^*$ 169.5 eV in DA-CCP-1, and S $2p_{1/2}^*$ 171.5 eV, and S $2p_{3/2}^*$ 170.2 eV in DA-CCP-2, respectively. In contrast, during the charging process, Zn^{2+} was dissociated from the DA-CCP-1 and -2 based cathodes and returned to the Zn anode resulting in almost complete recovery of the initial chemical shifts of thiophene-S. The XPS of Zn element in DA-CCP-1 and -2 provided further information about the nature of chemical species evolution during the charge and discharge processes (Fig. S29†). In the XPS profile of the discharged DA-CCP-1 and -2 electrodes (0.2 V *vs.* Zn/Zn^{2+}), the peaks at the binding energies of 1023.3 eV and 1046.5 eV can be assigned to Zn $2p_{3/2}$ and Zn $2p_{1/2}$ in Zn-thiophene-S of DA-CCP-1 and -2, respectively. Moreover, the Zn 2p doublet separations of the Zn-thiophene-S coordination complex in Fig. S29† appeared at 1023.2 eV, being

in good agreement with previously reported values for zinc ions binding to sulphur ions in ZnS lattices.[69,70] The fact that after the charging process only a decrease in the S–Zn and Zn signals is obtained may be associated with a highly irreversible process. However, *via* electrochemical analysis (*i.e.*, cyclability for 1000 cycles) we proved that the Zn^{2+} storage though DA-CCP-1 and -2 cathodes is highly reversible. Therefore, other techniques with a higher penetration depth, such as attenuated total reflection-Fourier-transform infrared spectroscopy (ATR-FTIR), should be used to ascertain the electrochemical reversibility. Therefore, we designed an ATR-FTIR battery to investigate the mechanism of Zn ion uptake/removal from DA-CCP-1 and -2. The main difference from the Zn-HSC fabrication is that DA-CCP-1 and -2 were coated onto a tailored stainless-steel mesh because infrared (IR) light can penetrate the cathode allowing *in situ* FTIR analysis (Fig. S30a†). Fig. S30b and c† show the FTIR spectra of DA-CCP-1 and -2 in the pristine, discharged, and charged states of DA-CCP-1 and -2 respectively. The stretching vibration at ~876 cm^{-1} can be ascribed to the C–S sulfur signal in thiophene-S.[71] During the discharge process a new band appears at ~1025 cm^{-1} and can be attributed to the formation of a S–Zn coordination bond (Fig. S30b and c†). When the electrodes are recharged again to 1.6 V, the C–S vibration is recovered for both DA-CCP-1 and -2, confirming the reversible nature of the interactions between the electrode materials and Zn ions. Nonetheless, the presence of the C–S–Zn signal in the charged state is monitored and can be ascribed to the irreversible trapping of Zn within the DA-CCP-1 and -2 matrices that takes place during the first charging/discharging cycles in agreement with cyclability analysis (Fig. 4c and f).
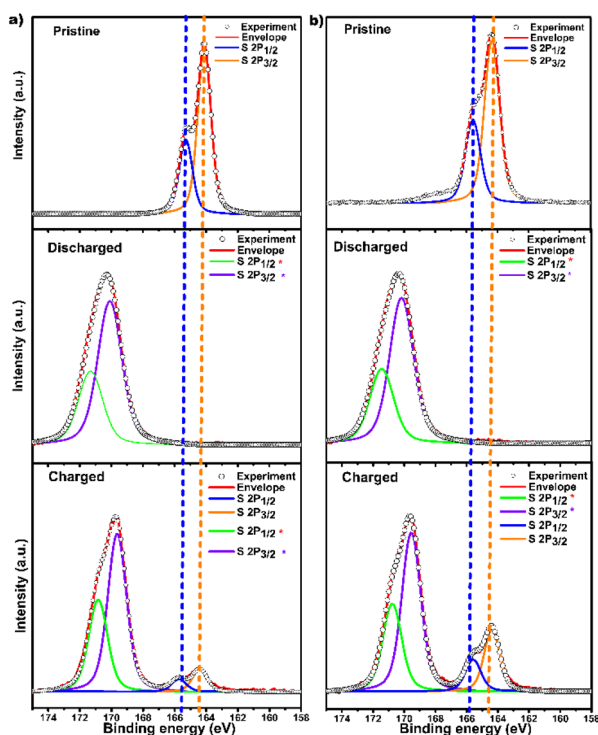
Conclusions

In summary, we have synthesized two novel thiophene-bridged carbon-linked conjugated polymers DA-CCP-1 and -2, as suitable novel cathode materials for Zn-HSCs. Due to the robust carbon-linked conjugations, high surface area (584 and 674 m^2 g^{-1}, respectively), donor–acceptor semiconducting structures, and thiophene-S active sites, the DA-CCP-1 and -2 electrode-based Zn-HSCs showed key performance indicators surpassing the state of the art. In particular, they displayed a pseudocapacitive Zn^{2+} storage behaviour with high capacity (103.4 and 251.7 mA h g^{-1}, respectively), energy density (80.6 and 196.3 W h kg^{-1}, respectively), power density (8.3 and 20.5 kW kg^{-1}, respectively), fast rate capability (up to 5 A g^{-1} in both cases), and long cycling stability (capacity retention of 96.2% and 84.5%, respectively, after >1000 cycles). *Ex situ* XPS and FTIR analysis revealed that the thiophene-S units of DA-CCP-1 and -2 act as the electrochemically active centres for Zn^{2+} storage in Zn-HSCs. Thiophene-bridged DA-CCP-1 and -2 hold potential to become powerful scaffolds for a wide variety of applications in energy storage, especially in Li–S batteries, gas storage, photocatalysis, *etc.* In addition, due to their unique inherent structural features, they could become powerful active materials for chemical sensing and gas separation.

Fig. 5 XPS analysis of thiophene–S units in pristine, charged, and discharged states of (a) DA-CCP-1 and (b) DA-CCP-2 cathodes, respectively.

This journal is © The Royal Society of Chemistry 2023

J. Mater. Chem. A, 2023, **11**, 2718–2725 | **2723**

Conflicts of interest

There are no conflicts to declare.

Acknowledgements

References

1 J. R. Miller and P. Simon, *Science*, 2008, **321**, 651.

2 P. Simon and Y. Gogotsi, *Nat. Mater.*, 2008, **7**, 845–854.

3 P. Zhang, F. Wang, M. Yu, X. Zhuang and X. Feng, *Chem. Soc. Rev.*, 2018, **47**, 7426–7451.

4 J. M. Tarascon and M. Armand, *Nature*, 2001, **414**, 359–367.

5 V. Etacheri, R. Marom, R. Elazari, G. Salitra and D. Aurbach, *Energy Environ. Sci.*, 2011, **4**, 3243–3262.

6 M. N. Obrovac and V. L. Chevrier, *Chem. Rev.*, 2014, **114**, 11444–11502.

7 J. B. Goodenough and K.-S. Park, *J. Am. Chem. Soc.*, 2013, **135**, 1167–1176.

8 F. Wang, X. Wu, X. Yuan, Z. Liu, Y. Zhang, L. Fu, Y. Zhu, Q. Zhou, Y. Wu and W. Huang, *Chem. Soc. Rev.*, 2017, **46**, 6816–6854.

9 E. Pomerantseva, F. Bonaccorso, X. Feng, Y. Cui and Y. Gogotsi, *Science*, 2019, **366**, eaan8285.

10 D. P. Dubal, O. Ayyad, V. Ruiz and P. Gómez-Romero, *Chem. Soc. Rev.*, 2015, **44**, 1777–1790.

11 M. R. Lukatskaya, B. Dunn and Y. Gogotsi, *Nat. Commun.*, 2016, **7**, 12647.

12 P. Zhang, Y. Li, G. Wang, F. Wang, S. Yang, F. Zhu, X. Zhuang, O. G. Schmidt and X. Feng, *Adv. Mater.*, 2019, **31**, 1806005.

13 G. Li, Z. Yin, H. Guo, Z. Wang, G. Yan, Z. Yang, Y. Liu, X. Ji and J. Wang, *Adv. Energy Mater.*, 2019, **9**, 1802878.

14 Y. Ma, H. Chang, M. Zhang and Y. Chen, *Adv. Mater.*, 2015, **27**, 5296–5308.

15 C. Sun, X. Zhang, C. Li, K. Wang, X. Sun and Y. Ma, *Energy Storage Mater.*, 2020, **24**, 160–166.

16 *COM(2020)474, Communication Critical Raw Materials Resilience: Charting a Path towards Greater Security and Sustainability*.

17 Z. Li, D. Chen, Y. An, C. Chen, L. Wu, Z. Chen, Y. Sun and X. Zhang, *Energy Storage Mater.*, 2020, **28**, 307–314.

18 Z. Li, Y. An, S. Dong, C. Chen, L. Wu, Y. Sun and X. Zhang, *Energy Storage Mater.*, 2020, **31**, 252–266.

19 L. Dong, X. Ma, Y. Li, L. Zhao, W. Liu, J. Cheng, C. Xu, B. Li, Q.-H. Yang and F. Kang, *Energy Storage Mater.*, 2018, **13**, 96–102.

20 H. Li, C. Han, Y. Huang, Y. Huang, M. Zhu, Z. Pei, Q. Xue, Z. Wang, Z. Liu, Z. Tang, Y. Wang, F. Kang, B. Li and C. Zhi, *Energy Environ. Sci.*, 2018, **11**, 941–951.

21 W. Sun, F. Wang, B. Zhang, M. Zhang, V. Küpers, X. Ji, C. Theile, P. Bieker, K. Xu, C. Wang and M. Winter, *Science*, 2021, **371**, 46.

22 P. Ruan, S. Liang, B. Lu, H. J. Fan and J. Zhou, *Angew. Chem., Int. Ed.*, 2022, e202200598.

23 H. Wang, M. Wang and Y. Tang, *Energy Storage Mater.*, 2018, **13**, 1–7.

24 J. Han, K. Wang, W. Liu, C. Li, X. Sun, X. Zhang, Y. An, S. Yi and Y. Ma, *Nanoscale*, 2018, **10**, 13083–13091.

25 K. W. Nam, H. Kim, Y. Beldjoudi, T.-w. Kwon, D. J. Kim and J. F. Stoddart, *J. Am. Chem. Soc.*, 2020, **142**, 2541–2548.

26 M. Yu, N. Chandrasekhar, R. K. M. Raghupathy, K. H. Ly, H. Zhang, E. Dmitrieva, C. Liang, X. Lu, T. D. Kühne, H. Mirhosseini, I. M. Weidinger and X. Feng, *J. Am. Chem. Soc.*, 2020, **142**, 19570–19578.

27 J.-S. M. Lee and A. I. Cooper, *Chem. Rev.*, 2020, **120**, 2171–2214.

28 H. Zhang, L. Zhong, J. Xie, F. Yang, X. Liu and X. Lu, *Adv. Mater.*, 2021, **33**, 2101857.

29 J. Chen, W. Yan, E. J. Townsend, J. Feng, L. Pan, V. Del Angel Hernandez and C. F. J. Faul, *Angew. Chem., Int. Ed.*, 2019, **58**, 11715–11719.

30 J. Roncali, *J. Mater. Chem.*, 1999, **9**, 1875–1893.

31 P. M. DiCarmine, T. B. Schon, T. M. McCormick, P. P. Klein and D. S. Seferos, *J. Phys. Chem. C*, 2014, **118**, 8295–8307.

32 Q. Huang, J. Chen, S. Yan, X. Shao, Y. Dong, J. Liu, W. Li and C. Zhang, *ACS Sustainable Chem. Eng.*, 2021, **9**, 13807–13817.

33 P. Murto, S. Elmas, U. A. Méndez-Romero, Y. Yin, Z. Genene, M. Mone, G. G. Andersson, M. R. Andersson and E. Wang, *Macromolecules*, 2020, **53**, 11106–11119.

34 H. Zhang, M. Yao, J. Wei, Y. Zhang, S. Zhang, Y. Gao, J. Li, P. Lu, B. Yang and Y. Ma, *Adv. Energy Mater.*, 2017, **7**, 1701063.

35 S. Xu, Y. Li, B. P. Biswal, M. A. Addicoat, S. Paasch, P. Imbrasas, S. Park, H. Shi, E. Brunner, M. Richter, S. Lenk, S. Reineke and X. Feng, *Chem. Mater.*, 2020, **32**, 7985–7991.

36 T. Huang, X. Lin, Y. Liu, J. Zhao, H. Lin, Z. Xu, S. Zhong, C. Zhang, X. Wang, X. Fu and J. Long, *ChemSusChem*, 2020, **13**, 672–676.

37 S. Xu, H. Sun, M. Addicoat, B. P. Biswal, F. He, S. Park, S. Paasch, T. Zhang, W. Sheng, E. Brunner, Y. Hou, M. Richter and X. Feng, *Adv. Mater.*, 2021, **33**, 2006274.

38 S. Xu, G. Wang, B. P. Biswal, M. Addicoat, S. Paasch, W. Sheng, X. Zhuang, E. Brunner, T. Heine, R. Berger and X. Feng, *Angew. Chem., Int. Ed.*, 2019, **58**, 849–853.

39 H. Wang, M. Wang and Y. Tang, *Energy Storage Mater.*, 2018, **13**, 1–7.

40 H. Zhang, Q. Liu, Y. Fang, C. Teng, X. Liu, P. Fang, Y. Tong and X. Lu, *Adv. Mater.*, 2019, **31**, 1904948.

41 F. Blanc, S. Y. Chong, T. O. McDonald, D. J. Adams, S. Pawsey, M. A. Caporini and A. I. Cooper, *J. Am. Chem. Soc.*, 2013, **135**, 15290–15293.

2724 | *J. Mater. Chem. A*, 2023, **11**, 2718–2725

This journal is © The Royal Society of Chemistry 2023

42 M. Wilhelm, M. Neidhöfer, S. Spiegel and H. W. Spiess, *Macromol. Chem. Phys.*, 1999, **200**, 2205–2207.

43 J. Lin, S. Bi, Z. Fan, Z. Fu, Z. Meng, Z. Hou and F. Zhang, *Polym. Chem.*, 2021, **12**, 1661–1667.

44 X. L. Wu and K. W. Zilm, *J. Magn. Reson.*, 1993, **102**, 205–213.

45 Y. Zhao, H. Liu, C. Wu, Z. Zhang, Q. Pan, F. Hu, R. Wang, P. Li, X. Huang and Z. Li, *Angew. Chem., Int. Ed.*, 2019, **58**, 5376–5381.

46 A. Yassin, M. Trunk, F. Czerny, P. Fayon, A. Trewin, J. Schmidt and A. Thomas, *Adv. Funct. Mater.*, 2017, **27**, 1700233.

47 S. Bi, Z.-A. Lan, S. Paasch, W. Zhang, Y. He, C. Zhang, F. Liu, D. Wu, X. Zhuang, E. Brunner, X. Wang and F. Zhang, *Adv. Funct. Mater.*, 2017, **27**, 1703146.

48 X. Zhuang, W. Zhao, F. Zhang, Y. Cao, F. Liu, S. Bi and X. Feng, *Polym. Chem.*, 2016, **7**, 4176–4181.

49 W. Zhao, S. Han, X. Zhuang, F. Zhang, Y. Mai and X. Feng, *J. Mater. Chem. A*, 2015, **3**, 23352–23359.

50 H. Zhang, L. Zhong, J. Xie, F. Yang, X. Liu and X. Lu, *Adv. Mater.*, 2021, 2101857.

51 P. Makuła, M. Pacia and W. Macyk, *J. Phys. Chem. Lett.*, 2018, **9**, 6814–6817.

52 S. Xu, H. Sun, M. Addicoat, B. P. Biswal, F. He, S. Park, S. Paasch, T. Zhang, W. Sheng, E. Brunner, Y. Hou, M. Richter and X. Feng, *Adv. Mater.*, 2020, 2006274.

53 J. Weber, M. Antonietti and A. Thomas, *Macromolecules*, 2008, **41**, 2880–2885.

54 N. Zhang, F. Cheng, Y. Liu, Q. Zhao, K. Lei, C. Chen, X. Liu and J. Chen, *J. Am. Chem. Soc.*, 2016, **138**, 12894–12901.

55 J. Ji, L. L. Zhang, H. Ji, Y. Li, X. Zhao, X. Bai, X. Fan, F. Zhang and R. S. Ruoff, *ACS Nano*, 2013, **7**, 6237–6243.

56 C. Yuan, J. Li, L. Hou, X. Zhang, L. Shen and X. W. Lou, *Adv. Funct. Mater.*, 2012, **22**, 4592–4597.

57 X. Wu, J. J. Hong, W. Shin, L. Ma, T. Liu, X. Bi, Y. Yuan, Y. Qi, T. W. Surta, W. Huang, J. Neuefeind, T. Wu, P. A. Greaney, J. Lu and X. Ji, *Nat. Energy*, 2019, **4**, 123–130.

58 T. Sun, Z.-J. Li, Y.-F. Zhi, Y.-J. Huang, H. J. Fan and Q. Zhang, *Adv. Funct. Mater.*, 2021, **31**, 2010049.

59 K. A. Owusu, X. Pan, R. Yu, L. Qu, Z. Liu, Z. Wang, M. Tahir, W. A. Haider, L. Zhou and L. Mai, *Mater. Today Energy*, 2020, **18**, 100529.

60 S. Wang, Z. Yuan, X. Zhang, S. Bi, Z. Zhou, J. Tian, Q. Zhang and Z. Niu, *Angew. Chem., Int. Ed.*, 2021, **60**, 7056–7060.

61 J. Xie, F. Yu, J. Zhao, W. Guo, H.-L. Zhang, G. Cui and Q. Zhang, *Energy Storage Mater.*, 2020, **33**, 283–289.

62 S. Wang, Q. Wang, P. Shao, Y. Han, X. Gao, L. Ma, S. Yuan, X. Ma, J. Zhou, X. Feng and B. Wang, *J. Am. Chem. Soc.*, 2017, **139**, 4258–4261.

63 S. Gu, S. Wu, L. Cao, M. Li, N. Qin, J. Zhu, Z. Wang, Y. Li, Z. Li, J. Chen and Z. Lu, *J. Am. Chem. Soc.*, 2019, **141**, 9623–9628.

64 D. Kundu, B. D. Adams, V. Duffort, S. H. Vajargah and L. F. Nazar, *Nat. Energy*, 2016, **1**, 16119.

65 C. Xu, B. Li, H. Du and F. Kang, *Angew. Chem., Int. Ed.*, 2012, **51**, 933–935.

66 H. Pan, Y. Shao, P. Yan, Y. Cheng, K. S. Han, Z. Nie, C. Wang, J. Yang, X. Li, P. Bhattacharya, K. T. Mueller and J. Liu, *Nat. Energy*, 2016, **1**, 16039.

67 Y. Su, Z. Yao, F. Zhang, H. Wang, Z. Mics, E. Cánovas, M. Bonn, X. Zhuang and X. Feng, *Adv. Funct. Mater.*, 2016, **26**, 5893–5902.

68 B. Quan, S.-H. Yu, D. Y. Chung, A. Jin, J. H. Park, Y.-E. Sung and Y. Piao, *Sci. Rep.*, 2014, **4**, 5639.

69 X. Li, X. Li, B. Zhu, J. Wang, H. Lan and X. Chen, *RSC Adv.*, 2017, **7**, 30956–30962.

70 Y.-C. Liang and C.-C. Wang, *RSC Adv.*, 2018, **8**, 5063–5070.

71 M. Hatamzadeh and M. Jaymand, *RSC Adv.*, 2014, **4**, 16792–16802.

This journal is © The Royal Society of Chemistry 2023

J. Mater. Chem. A, 2023, **11**, 2718–2725 | **2725**